Large-scale molecular dynamics simulations of glancing angle deposition

Bradley C. Hubartt, Xuejing Liu, and Jacques G. Amar

Citation: J. Appl. Phys. **114**, 083517 (2013); doi: 10.1063/1.4819446
View online: http://dx.doi.org/10.1063/1.4819446
View Table of Contents: http://jap.aip.org/resource/1/JAPIAU/v114/i8
Published by the AIP Publishing LLC.

JOURNAL OF APPLIED PHYSICS **114**, 083517 (2013)

Large-scale molecular dynamics simulations of glancing angle deposition

Bradley C. Hubartt, Xuejing Liu, and Jacques G. Amar
Department of Physics and Astronomy, University of Toledo, Toledo, Ohio 43606, USA

(Received 2 May 2013; accepted 13 August 2013; published online 28 August 2013)

Using a computationally efficient method, we have carried out large-scale molecular dynamics simulations of Cu/Cu(100) growth up to 20 monolayers (ML) for deposition angles ranging from 50° to 85° and for both random and fixed azimuthal angles. A variety of quantities including the porosity, roughness, lateral correlation length, average grain size, strain, and defect concentration are used to characterize the thin-film morphology. For large deposition angles ($\theta \geq 80°$), we find well-defined columnar growth while for smaller angles, columnar growth has not yet set in. In addition, for $\theta = 70° - 85°$, the thin-film porosity and columnar tilt angles (for fixed azimuthal angle ϕ) are in reasonable agreement with experiments. For both random and fixed ϕ, the number of grains, average grain-size, and number of surface atoms belonging to (111) facets increase rapidly with deposition angle. As a result, twin facet formation and budding occur in our simulations, in good agreement with experiments. In good qualitative agreement with recent experimental observations, we also find that the average strain is initially compressive but becomes tensile after the onset of columnar growth. Our simulations also reveal that for large deposition angles a variety of unexpected and complex dynamical processes play a key role in determining the evolution of the surface morphology and microstructure. In particular, due to the existence of deposition-induced events, the vacancy density remains very small, even though the defect density is relatively large and increases with deposition angle. In addition, large-scale re-arrangement events as well as thermal (elastic) vibrations lead to large-amplitude oscillations in the columnar growth regime. These oscillations play a key role in promoting rapid coalescence via additional large-scale collective motion, thus, significantly enhancing the coarsening process.
[http://dx.doi.org/10.1063/1.4819446]

I. INTRODUCTION

Glancing angle deposition (GLAD) is a commonly used physical vapor deposition technique which may be used to produce sculptured thin-films with a variety of different morphological, electrical, and chemical properties.[1,2] In this technique, atoms are typically deposited at a large angle θ with respect to the substrate normal while the azimuthal angle ϕ may either be held fixed to produce tilted nanocolumns, continuously rotated to produce vertical columnar growth, or manipulated in a more complicated manner to produce nanostructures such as nanosprings. As a result, glancing-angle deposited thin-films have potential applications[2,3] in a variety of different areas including sensors, hydrogen storage, antireflective coatings, fuel-cells, magnetic storage devices, and solar cells.

Due to the dominant influence of shadowing on the thin-film morphology, a variety of simplified models[4,5] (corresponding to growth on a simple-cubic lattice) have been successfully used to model the dependence of the overall thin-film morphology on deposition angle. However, a variety of other important aspects such as the crystalline structure, grain boundaries, and defects, as well as deposition-triggered events[6,7] and concerted activated events are not included in these simulations. In addition, while a kinetic Monte Carlo model (ADEPT) for polycrystalline Al growth[8] has recently been developed which approximately takes into account grain orientation and grain boundaries by using multiple lattices, due to the lattice restriction this model does not take into account strain effects during growth, deposition-triggered events,[6,7] or concerted activated events.

While limited in time-scales, molecular dynamics (MD) simulations can realistically take into account all of these aspects of glancing-angle deposition thin-film growth. In addition, we note that recent experiments on GLAD of different metals as a function of temperature,[9] demonstrate the existence of scaling of the typical column width as a function of the homologous temperature T/T_m, where T is the deposition temperature and T_m is the melting temperature. Accordingly, we expect that the results of molecular dynamics simulations may be relevant to experiments carried out with significantly lower deposition rates but at a significantly lower temperature. However, due to the existence of multiple scattering at large deposition angles, carrying out molecular dynamics simulations of glancing angle deposition over extended length-scales can be quite challenging. Accordingly, we have developed a computationally efficient method (based on the use of a single graphical processing unit or GPU) to simulate the deposition process at large deposition angles.

Using this method, we have carried out large-scale MD simulations of GLAD of Cu/Cu(100) at 300 K, in order to study the dependence of the morphology and crystal structure on deposition angle both with and without substrate rotation. In agreement with experiments, for large deposition angles ($\theta \geq 80°$), we find well-defined columnar growth with vertical (tilted) columns for random (fixed) ϕ, while for $\theta = 70° - 85°$ the thin-film porosity and columnar tilt angles

(for fixed ϕ) are in reasonable agreement with experiments. In addition, we find that while the average strain is initially compressive for both random and fixed ϕ, it becomes tensile after the onset of columnar growth, in good qualitative agreement with recent experimental observations.[10] Our results also indicate that even on MD time-scales a variety of complex dynamical processes including coalescence, large-scale collective events, and budding play a key role in determining the evolution of the surface morphology and microstructure.

This paper is organized as follows. In Sec. II, we first discuss our simulation methods and parameters as well as the quantities measured. We then present our results for the evolution of the thin-film morphology and microstructure as a function of film thickness and deposition angle, for the case of both fixed and random azimuthal angle in Sec. III. Finally, we summarize our results in Sec. IV.

II. SIMULATIONS

A. Simulation parameters and methods

In our simulations, we have used an embedded-atom-method (EAM)[11] potential for Cu developed by Mishin *et al.*[12] which has been parameterized to reproduce the *ab initio* values of stacking fault and (111) twin energies. In order to minimize finite-size effects, we have used a relatively large system size corresponding to an initial square Cu(100) substrate of width $L = 80\ a$ (where a is the lattice constant of Cu) with 3 (bottom) fixed layers, 5 (middle) constant-temperature layers, and 2 (top) moving layers. A Langevin thermostat with a friction coefficient of $10^{12}\,\mathrm{s}^{-1}$ was used for the constant temperature layers while periodic boundary conditions were assumed parallel to the substrate. In order to study the dependence on deposition conditions, we have carried out simulations for deposition angles θ ranging from $\theta = 50^\circ$ to $\theta = 85^\circ$, as well as for both fixed azimuthal angle ϕ (corresponding to deposition along the [100] direction) and random ϕ (corresponding to a rotating substrate). Our simulations were carried out at 300 K while a total of 20 monolayers (ML) corresponding to 256 000 atoms were deposited in each case. In order to maximize computational efficiency, our simulations were carried out using a single GPU along with the public domain software HOOMD-blue,[13–15] which provides an efficient implementation of molecular dynamics on GPUs for a variety of different potentials.

In our simulations, 1/200 ML (corresponding to 64 atoms) was deposited in each deposition step or cycle, while to avoid interactions a sublattice was used (see Fig. 1). In particular, the area above the growing film was divided into an 8×8 grid which was further divided into 4 sublattices, A, B, C, and D (see Fig. 1). At the beginning of each deposition cycle, one of the sublattices is randomly selected and within each sublattice an initial (x, y) coordinate is randomly selected. The initial z-coordinate was determined by adding the cutoff distance to the highest z-coordinate in the film. Each depositing atom was then "launched" with the appropriate deposition and azimuthal angle, with an initial kinetic energy of 0.2 eV (corresponding to $K_i = 2k_BT_m$ where T_m is the melting temperature of Cu). We note that the use of a grid with sublattices ensures that the initial distance between depositing atoms is larger than $5a$ or approximately 18 Å.

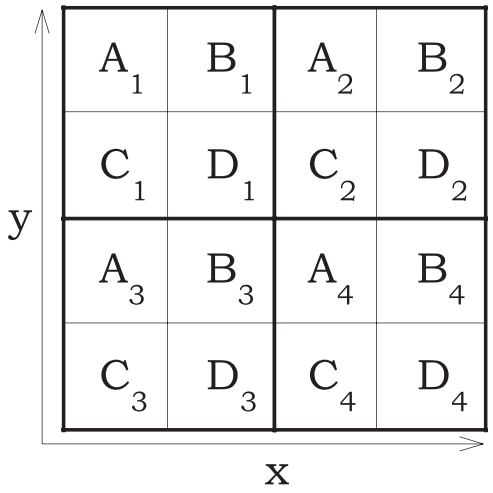

FIG. 1. Schematic showing 2×2 portion of 8×8 grid (along with A, B, C, and D sublattices) used to determine initial x, y coordinates of depositing atoms in each cycle.

In order to efficiently take multiple scattering of depositing atoms by the growing film into account, in each deposition cycle, an alternating sequence of processes consisting of ballistic deposition of all depositing atoms until they are within a cutoff distance from the substrate, followed by molecular dynamics simulations of the entire system for 1000 MD steps is carried out. In order to ensure accurate evolution during deposition, a relatively short time-step (0.41 fs) is used. This sequence of ballistic deposition and molecular dynamics was repeated until all of the depositing atoms were able to satisfy a landing criterion for two 1000 MD-step sequences. We note that to be considered to have "landed" an atom was required to move less than 1.5 Å from its initial position (roughly 60% of the nearest-neighbor distance for Cu) at the end of two successive 1000 MD-step sequences. Once all depositing atoms have landed, an additional 5000 MD steps were performed. We then increased the time-step to 3.2 fs and continued performing MD of the entire system until a total MD time of 16.4 ps had elapsed during each deposition cycle (corresponding to a deposition rate of 0.3 ML/ns). We note that when running on a single central processing unit (CPU) each of our simulations would have required over 15 000 h of CPU time which is significantly larger than the few hundred hours required when using a GPU.

B. Quantities measured

In order to analyze the surface morphology, we have measured a variety of quantities, including the root-mean-square height fluctuation or roughness

$$w = \frac{1}{N_c^{1/2}} \left[\Sigma_{i=1}^{N_c} (h(\mathbf{r_i}) - \bar{h})^2\right]^{1/2}, \quad (1)$$

where $h(\mathbf{r_i})$ is the maximum height z_i above the substrate of all the atoms in column i at position $\mathbf{r_i} = (x_i, y_i)$ along the substrate plane and $N_c = 160^2$ is the number of columns.

Here, we have mapped the (x, y) coordinates of each atom to the nearest point on a 160×160 square grid of box-size $a/2$ and $\bar{h}$ is the average film height. In addition, we have calculated the porosity

$$P = 1 - \frac{N_{dep} V_{atom}}{h_{max} L^2}, \tag{2}$$

where h_{max} is the maximum height of the film above the substrate, N_{dep} is the total number of atoms deposited, and $V_{atom} = a^3/4$ is the volume per atom in an fcc crystal. For the case of random azimuthal angle (corresponding to vertical columnar growth), we have also calculated the circularly averaged height-height correlation function

$$G(r) = \langle \tilde{h}(0)\tilde{h}(r) \rangle_C, \tag{3}$$

where $\tilde{h}(r) = h(r) - \bar{h}$ and the brackets denote a circular average over all directions, as well as the lateral correlation length $\xi = r_{min}$ where $G(r_{min})$ is the minimum value of $G(r)$.

In order to analyze the thin-film microstructure, we have also measured a variety of other quantities. In particular, in order to distinguish between bulk, surface, and/or defect atoms for each atom i of the film we have calculated the centrosymmetry parameter $\rho_{CS}(i)$, defined by[16]

$$\rho_{CS}(i) = \frac{1}{a} \Sigma_{j=1} |\vec{R}_j + \vec{R}_{j+6}|^2, \tag{4}$$

where R_j and R_{j+6} are the vectors corresponding to the six pairs of most opposite nearest atoms. Using this parameter, atoms were then classified as either bulk atoms ($\rho_{CS} < 0.03$), dislocation atoms ($0.03 < \rho_{CS} < 0.075$), stacking fault atoms ($0.075 < \rho_{CS} < 0.5$), or surface atoms ($\rho_{CS} > 1.25$). By counting the number of "bulk" atoms surrounded by defects, the average grain-size and grain-size distribution were also determined. In addition, we estimated the vacancy density by calculating the volume of empty regions surrounded by surface atoms within a grain, and dividing by the average volume per atom. In order to study the effects of deposition conditions on strain, we have also calculated the average strain $\bar{\epsilon} = \langle \epsilon_i \rangle$ as a function of film-thickness where $\epsilon_i = \frac{1}{a_1} \Sigma_{j=1}^{N} (|\mathbf{r_j} - \mathbf{r_i}|/N - a_1)$ is the local strain at atom i, a_1 is the nearest-neighbor distance of bulk Cu, and the sum is over the total number N of nearest-neighbors of atom i (corresponding to all atoms whose distances are within 20% of the bulk nearest-neighbor distance).

III. RESULTS

A. Morphology

Fig. 2 shows typical pictures of the surface morphology at coverage 10 ML and 15 ML for the case of random azimuthal angle. As can be seen, for moderate deposition angles ($\theta = 60^\circ$ or below), columnar growth has not yet set in, although the surface morphology becomes increasingly rough with increasing coverage. However, for larger deposition angles $\theta \geq 70^\circ$, a well-defined vertical columnar structure is beginning to develop, which becomes more pronounced with increasing deposition angle and film-thickness.

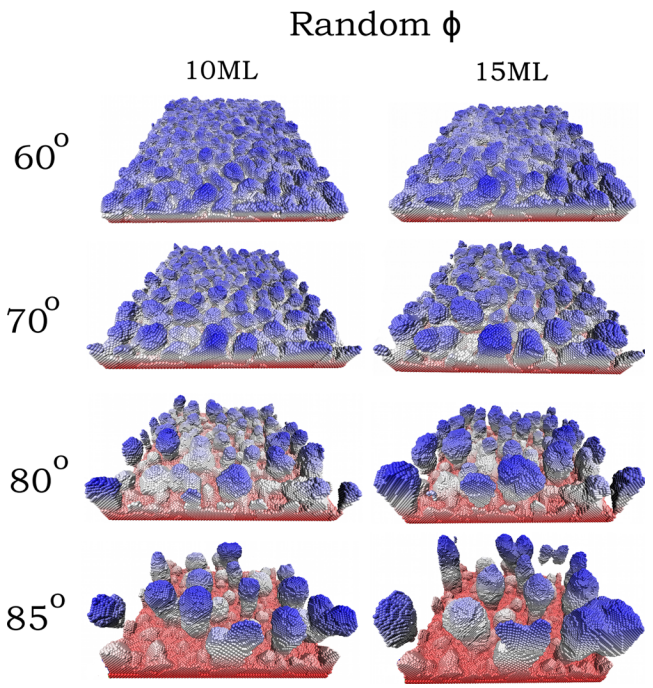

FIG. 2. Thin-film configurations for random azimuthal angle at 10 and 15 ML for $\theta = 60^\circ, 70^\circ, 80^\circ$, and 85°. Atoms are colored according to height above substrate.

In contrast, for fixed azimuthal angle (see Fig. 3) and moderate deposition angles $\theta = 50^\circ - 60^\circ$, ridge-like behavior with (100) cliffs running perpendicular to the deposition direction may be seen, as was previously found in Ref. 7. However, for larger deposition angles ($\theta = 70^\circ, 80^\circ$, and 85°), a well-defined columnar structure is again observed, which becomes more pronounced with increasing deposition angle and film-thickness. In this case, the columns are tilted in the deposition direction. Accordingly, we have measured the average tilt angle β corresponding to the angle between

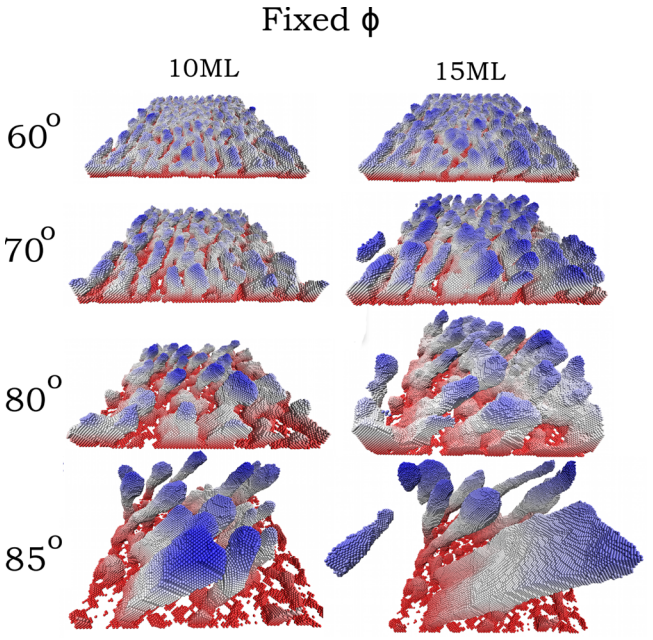

FIG. 3. Thin-film configurations for fixed azimuthal angle at 10 and 15 ML for $\theta = 60^\circ, 70^\circ, 80^\circ$, and 85°.

columns and the substrate normal at $t = 20$ ML for $\theta = 70°, 80°$, and $85°$ to be $42.8° \pm 8.3°, 49.33° \pm 7°$, and $39.6° \pm 11.6°$, respectively. Due to the existence of significant finite size effects for $\theta = 85°$ at higher coverage (see Fig. 3), the value is somewhat lower than expected. However, our two other values are close to the tilt angles measured in GLAD experiments by Suzuki and Taga,[5] e.g., $\beta = 43°$ at $\theta = 70°$ for both Ta_2O_5 and TiO_2, and $\beta = 53°$ at $\theta = 82°$ for Ta_2O_5.

We note that for both random and fixed ϕ, shadowing of smaller columns by larger columns as well as coalescence of nearby columns can be observed. Both of these processes lead to coarsening as the film-thickness increases. In particular, for $\theta = 85°$ with random ϕ (see Fig. 2), as the coverage increases from 10 ML to 15 ML the three columns in the bottom right corner of the system merge to form one column. In addition, for the case of random azimuthal angle, "budding" or splitting of a single column into two columns is also observed due to "twin" (111) facet formation (see back middle portion of pictures for $\theta = 85°$).[17]

Fig. 4 shows our results for the porosity P (averaged over 12–20 ML) as a function of deposition angle. As can be seen, the porosity increases significantly with increasing deposition angle although there is little difference between the results for fixed and random ϕ. In addition, as shown in the inset, for these angles, the porosity saturates relatively quickly after the first few layers. Also shown (dashed lines) are fits to experimental results of Poxson *et al.*[18] for SiO_2 and indium tin oxide (ITO) for fixed azimuthal angle, where we have used the Poxson *et al.*[18] fitting form $P_{exp} = \frac{\theta \tan\theta}{c + \theta \tan\theta}$ with $c = 3.17$ (3.55) for SiO_2 (ITO), respectively. For large deposition angles, there is good agreement between our simulation results and experiments. However, for smaller deposition angles, our porosity results are somewhat higher than the experimental values for SiO_2 and ITO, perhaps because fully columnar behavior has not yet been reached for these angles in our simulations.

Also shown in Fig. 4 are experimental results[19] for Cr and Cu GLAD films grown at room-temperature. While the experimental porosities for Cr films are somewhat lower than our simulation results, the experimental porosities for Cu films are significantly lower. The poorer agreement between our simulation results and experimental results for the porosity of metals at room temperature, along with the relatively good agreement for oxides, may be explained by the fact that due to the high deposition rates used in our simulations, our results are most relevant to experiments carried out with significantly lower deposition rates but at lower homologous temperatures T/T_m (where T_m is the corresponding melting temperature). This is consistent with the fact that the melting temperatures of Cr (2180 K) and SiO_2 (1873 K) are significantly higher than for Cu (1357 K).

The thin-film density as a function of height above the substrate, after 20 ML have been deposited, is shown in Fig. 5 for all deposition angles for the case of random ϕ. (Similar results have been obtained for fixed ϕ but are not shown for brevity.) As can be seen, for $\theta = 80°$ and $85°$, there is a well-defined region of constant density corresponding to columnar growth, while for smaller deposition angles ($\theta = 50°, 60°$, and $70°$) for which columnar growth is not yet fully defined by 20 ML, there is no well-defined region of constant density. Consistent with our porosity results, the maximum film height increases with increasing deposition angle.

In order to gain a better understanding of the surface morphology, we have also measured the roughness w as a function of film-thickness. As can be seen in Fig. 6, for random ϕ, the surface roughness increases approximately linearly, as expected for columnar growth. However, for fixed ϕ, the growth exponent β (where $w \sim t^{\beta}$ and t is the film thickness) is less than 1 for small deposition angles, but approaches 1 for $\theta = 80°$ and $85°$. (For $\theta = 85°$, the surface roughness is somewhat reduced for $t > 15$ ML due to finite-

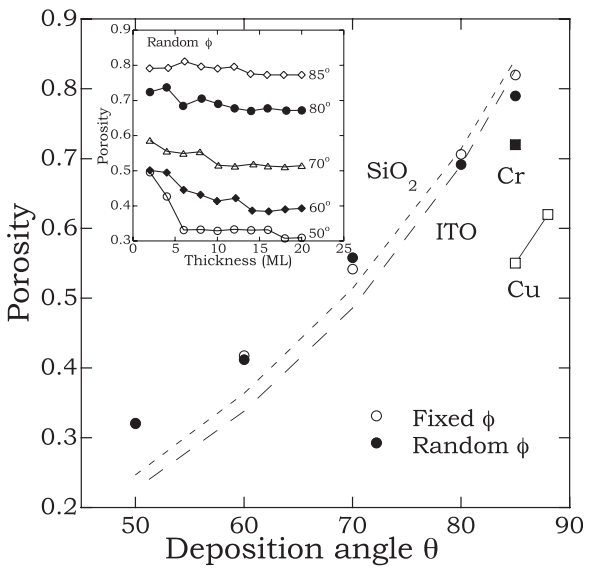

FIG. 4. Comparison of thin-film porosity obtained in simulations (open and filled circles) with fits to experimental results (dashed lines) for SiO_2 and ITO. Also shown are experimental results for Cu and Cr (open and filled squares). Inset: Porosity as a function of film thickness for random ϕ.

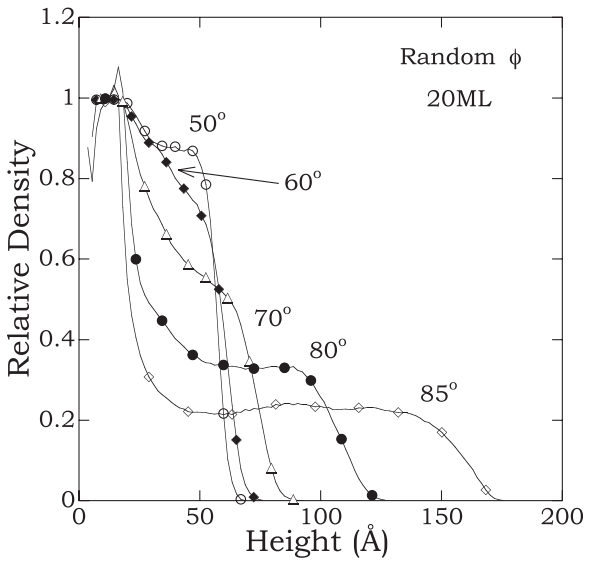

FIG. 5. Density profile (normalized to bulk density) of simulated films for random ϕ at 20 ML coverage.

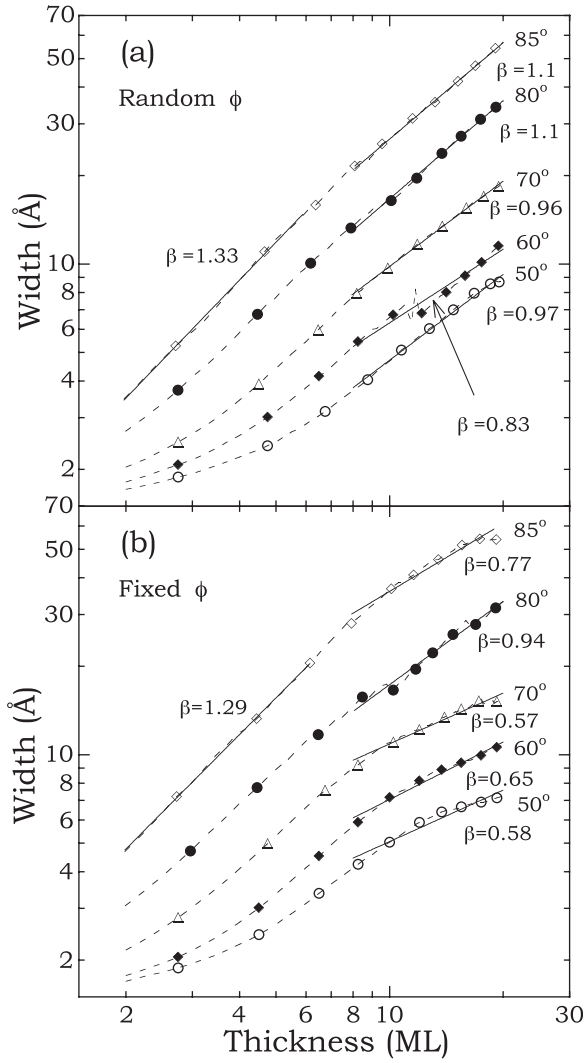

FIG. 6. Surface width as a function of film thickness for (a) random ϕ and (b) fixed ϕ.

size effects.) Interestingly, except for $\theta = 85°$, there is relatively good agreement between the roughness for the case of fixed azimuthal angle and that for random azimuthal angle (corresponding to substrate rotation[20]) over the entire range of coverage. We note that these results are in qualitative agreement with the results of recent smaller scale MD simulations[21] of the first few ML of Ti/Ti(100) growth.

The circularly averaged lateral correlation length ξ for random ϕ is shown in Fig. 7 as a function of deposition angle and film-thickness. For large deposition angles, the coarsening exponent n (where $\xi \sim t^n$) is approximately 1/2, in good agreement with previous GLAD simulation results using a simple-cubic lattice model in the absence of diffusion.[9,22] The large value of the coarsening exponent is also consistent with the increased amount of shadowing and coalescence which occurs at high deposition angles.

However, for smaller deposition angles, the coarsening exponents are significantly smaller ($n \simeq 0.2 - 0.33$) and are consistent with the values obtained in simulations with surface diffusion.[22] This is also consistent with the fact that for small deposition angles, almost all of the film atoms correspond to the same (substrate) grain. In contrast, we find that

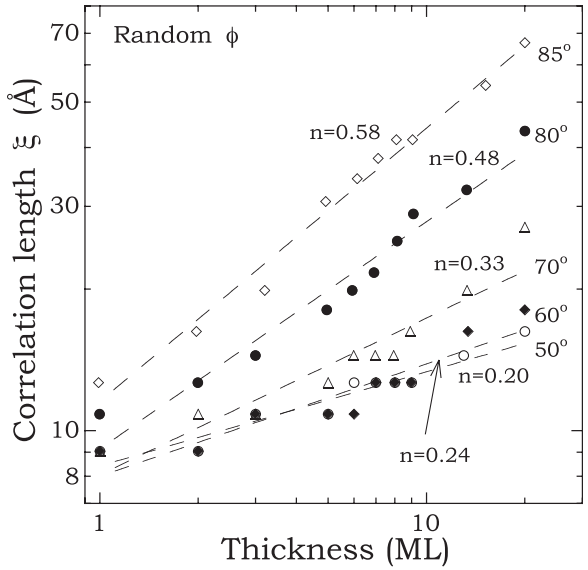

FIG. 7. Lateral correlation length as a function of film thickness for random ϕ.

the surface area growth exponent $\delta \simeq 0.5$ (where $S \sim t^{\delta}$ is the number of surface atoms) is independent of deposition angle.

B. Microstructure and strain

In order to study the microstructure, we have used the centrosymmetry parameter to classify film atoms as either surface atoms, defect atoms (corresponding to stacking faults and/or partial dislocations), or bulk atoms. Fig. 8(a) shows a typical picture of the grain structure for the case of $\theta = 85°$ and random ϕ at $t = 15$ ML. (Note that the configuration in this picture is the same as that shown in Fig. 2 but viewed from behind.) In this picture, only the bulk atoms, which have been colored to distinguish between different grains, are shown while the gaps between grains correspond to stacking fault atoms which have been removed from the image. In this case, approximately 90% of the deposited atoms do not belong to the initial (yellow) "substrate" grain. (In contrast, for $\theta = 50°$ and 15 ML, only approximately 35% of the deposited atoms correspond to defects or bulk atoms which do not belong to the substrate grain.)

Fig. 8(b) shows just the stacking fault atoms for this configuration. As can be seen, there are well-defined stacking fault planes. This is consistent with our nearest-neighbor analysis of the surface structure which indicates that for all deposition angles there are a relatively large number of (111) and (100) facets, although (111) facets dominate (see Fig. 8(a)) while the ratio of (111) facet atoms to (100) facet atoms increases with deposition angle. As can be seen in Fig. 8(a), for the case of $\theta = 85°$ and random ϕ well-defined (111) facets are clearly observed at a thickness of 15 ML. In this connection, an estimate of the (111) facet diffusion length in our simulations, e.g., $l \simeq \sqrt{D_h \tau} a_1$ (where a_1 is the Cu nearest-neighbor distance, $\tau = 3.3$ ns is the deposition time per ML and $D_h = 4.2 \times 10^{12}$ hops/s is the monomer hopping rate for the Mishin EAM potential at 300 K) gives a value ($69\, a_1$) which is somewhat larger than the maximum (111) facet diameter (approximately $20\, a_1$). This is also consistent

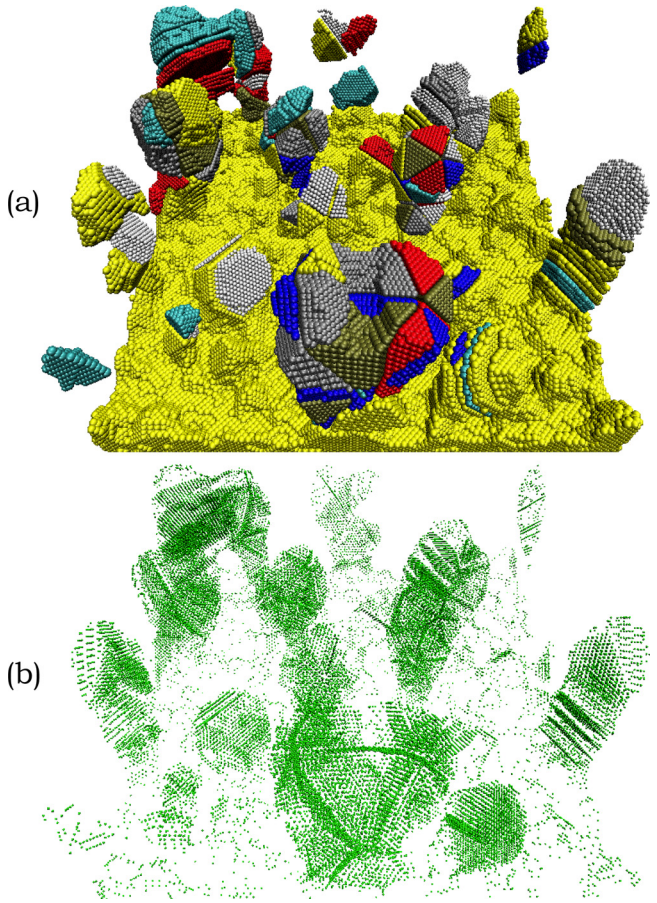

FIG. 8. (a) Grain structure of simulated film for $\theta = 85^\circ$ and random ϕ, at $t = 15$ ML. Only bulk atoms are shown and each grain is colored differently (but not uniquely) from its neighbors. (b) Same configuration as (a) but only stacking fault atoms are shown.

with the existence of significant 2D and 3D interlayer diffusion barriers at (111) step-edges.[23] We note that the Mishin EAM potential barrier for Cu/Cu(111) diffusion (0.041 eV (Ref. 24)) used here is in good agreement with the experimental value[25] of 0.037 ± 0.005.

Fig. 9 shows the evolution of the average (non-substrate) grain size (corresponding to the average number of atoms in a grain) as a function of coverage for the case of random ϕ and different deposition angles. As can be seen, both the average (non-substrate) grain size as well as the total number of grains (see inset) increase rapidly with both film thickness and deposition angle. Similar results have also been obtained for fixed ϕ. However, due to the fact that both shadowing and coalescence are more significant for fixed ϕ, in this case, the average grain size is significantly larger than for random ϕ while the number of grains is significantly smaller.

In order to more completely analyze the microstructure, we have also calculated the total defect atom fraction (including dislocations and stacking faults) as well as the vacancy volume fraction for random ϕ as shown in Fig. 10. As can be seen, due to the large deposition rate of 0.3 ML/ns the defect atom fraction is relatively large and increases (for large film thicknesses) with increasing deposition angle - ranging from a value at 20 ML of approximately 8% for $\theta = 50^\circ$ to 23% for $\theta = 85^\circ$. In addition, for large deposition angles $\theta \geq 80^\circ$ (corresponding to well-defined columnar

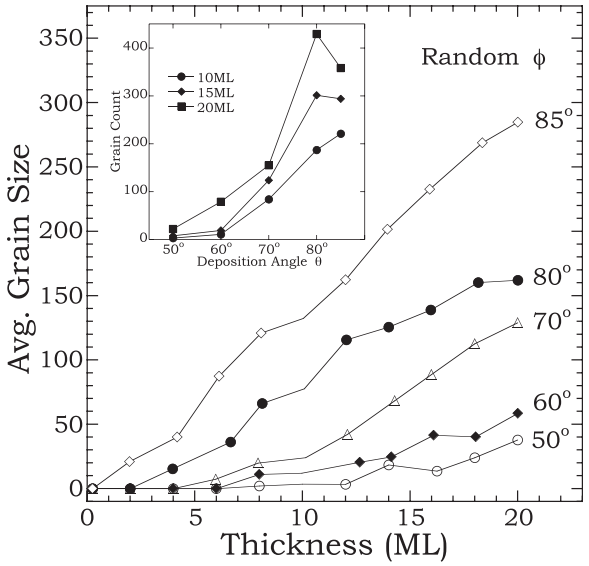

FIG. 9. Average grain size (not including large substrate grain) as function of film thickness for different deposition angles θ and random ϕ. Inset shows grain count at 10, 15, and 20 ML as function of deposition angle.

growth), the defect fraction increases monotonically with increasing film thickness. In contrast, for $\theta \leq 70^\circ$, the defect density first increases rapidly in the first 1–2 ML, then decreases with increasing coverage, and then increases more slowly with increasing coverage. This non-monotonic behavior may be due to the increased effects of deposition-induced events (see below) for smaller deposition angles (which leads to a smaller defect density and may also allow the defect density to decrease) combined with the reduced density of (111) facets, which reduces the density of stacking faults.

In contrast, while the vacancy fraction increases with deposition angle and film thickness, it appears to saturate at a relatively low value (approximately 0.001) which is independent of deposition angle. As we have previously shown in Ref. 7 for the case of low-temperature Cu/Cu(100) growth

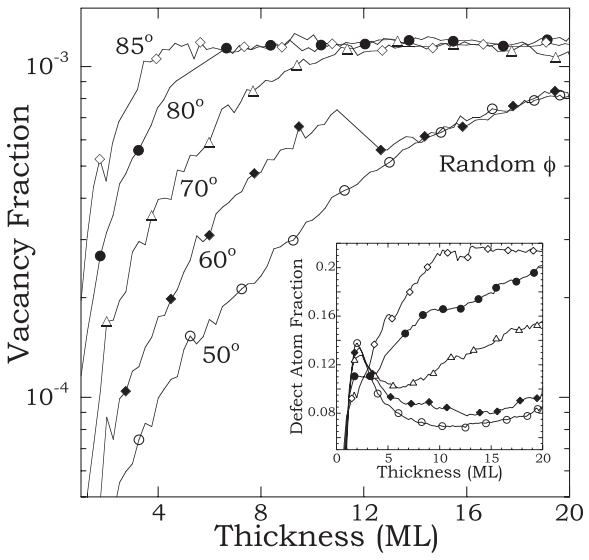

FIG. 10. Vacancy fraction as function of film-thickness and deposition angle for random ϕ. Total defect atom fraction is shown in inset.

with fixed ϕ and $\theta = 60^\circ$, this relatively small vacancy density may be explained by the existence of concerted deposition-induced events which eliminate vacancies even in the absence of thermally activated events, and which occur as a result of the relatively large[26–28] (approximately 2.3–3 eV) energy of condensation of depositing atoms. We note that similar results (not shown) were also obtained for the case of fixed ϕ and in this case the vacancy fraction was approximately the same.

We have also measured the average strain as a function of coverage and deposition angle. As can be seen in Fig. 11 for the case of random ϕ, while the strain is initially compressive for all deposition angles, for large deposition angles ($\theta = 80^\circ$ and 85°), it becomes tensile at larger thicknesses corresponding to columnar growth. Interestingly, for $\theta \geq 70^\circ$, the maximum compressive strain appears to correspond to the onset of a columnar morphology during the growth. Similar results have also been obtained (not shown) for the case of fixed azimuthal angle. The transition from compressive to tensile strain at the onset of columnar growth is qualitatively similar to the behavior obtained previously in Ref. 10 in sputter-deposition experiments on Be growth with and without substrate bias.

One possible explanation for the crossover from compressive to tensile strain is a competition among different stress generation and relaxation processes that take place at grain boundaries during film growth.[10] In particular, due in part to the initial kinetic energy of condensation, depositing atoms may be incorporated at grain boundaries[29] thus leading to compressive strain in the early stages of growth. However, since tensile stress is generated as grain boundaries grow,[30] then as the number and size of grain boundaries increase, the effects of tensile stress will become more important. As a result, the average strain crosses over from compressive to tensile with increasing film thickness and deposition angle. We note that this scenario is consistent with the results shown in Fig. 9 for the dependence of the average grain size and number of grains on deposition angle and film thickness. In particular, for deposition angles of 50° and 60° for which the number of grains and average grain size are both small (corresponding to a length-scale which is not much bigger than the typical size of a deposition-induced event), the overall strain remains compressive even at a thickness of 20 ML. In contrast, for larger deposition angles ($\theta \geq 70^\circ$) both the average grain-size and number of grains (e.g., grain boundaries) increase significantly with thickness, thus, leading to tensile strain.

C. Large-scale collective events: Rearrangement, coalescence, and budding

As indicated by our results for the evolution of the thin-film morphology (see Sec. III A) in the case of columnar growth ($\theta \geq 70^\circ$), the coalescence of nearby columnar structures plays an important role. Accordingly, in order to gain a better understanding of the coalescence process, we have carried out a careful examination of the evolution of the surface morphology in the columnar regime. Our results indicate that the growing nanocolumns undergo relatively large amplitude oscillations which are due to large-scale rearrangement events as well as thermal (elastic) vibrations. In addition, when two columns approach within a cutoff distance from one another, then rapid coalescence occurs as a result of additional large-scale collective motions which include rotation and tilting (see Fig. 12).

In order to quantify these oscillations, we have also carried out annealing simulations for the case of $\theta = 80^\circ$ with fixed ϕ and 15 ML thickness, and have found that these oscillations occur even in the absence of deposition. In contrast to the example shown in Fig. 12 for $\theta = 70^\circ$, in this case, due to the relatively large spacing of the nanocolumns at this thickness and deposition angle, no coalescence occurs during annealing. We find that the oscillation frequencies range from 4 GHz for a large column to 21 GHz for a smaller column. Surprisingly, for the large column, the oscillation amplitude is significantly larger than the calculated thermal

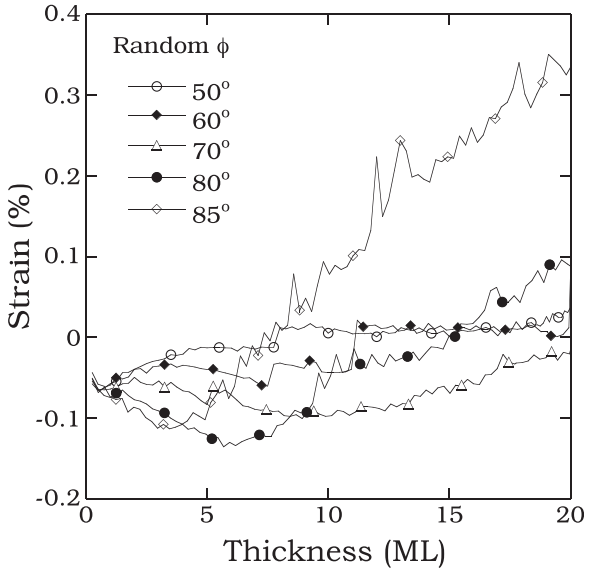

FIG. 11. Average strain as function of film-thickness and deposition angle for random ϕ.

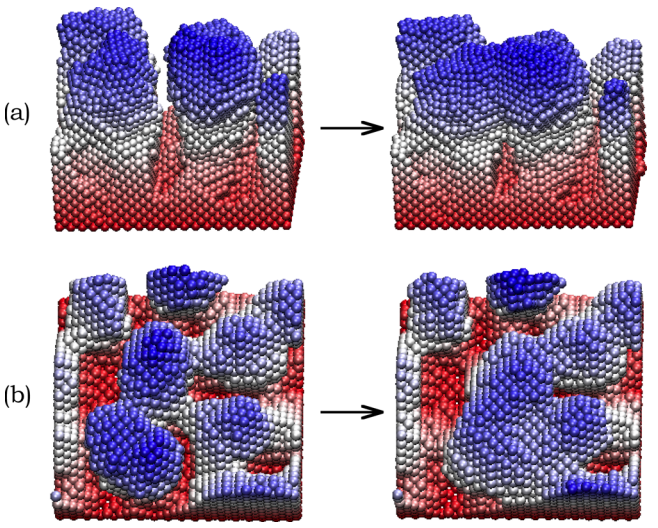

FIG. 12. Large-scale coalescence events for random ϕ and $\theta = 70^o$ which occur at approximately (a) 16.75 ML and (b) 11.5 ML. In each case, the interval between snapshots corresponds to 0.25 ML.

amplitude[31] for a bulk Cu nanocolumn with the same dimensions, while the oscillation frequency is correspondingly smaller. Both of these discrepancies can be explained by the existence of a reduced Young's modulus due to a high defect density. In contrast, for the small column, we find good agreement with the theoretical vibration amplitude and frequency using the Young's modulus for bulk Cu.

In contrast to the large-scale rearrangement and coalescence of nearby columns during growth, which enhance coarsening, we have also found that in the case of random azimuthal angle, splitting and/or budding of columns may also occur as shown in more detail in Fig. 13. Similar budding behavior has also been seen experimentally[17] and has previously been explained[17] as due to the existence of twin (111) facets combined with shadowing along with the existence of a large (0.40 eV) 3D Ehrlich-Schwoebel barrier[23,32,33] to interfacet diffusion. As can be seen by the orientation of the stacking faults shown in the front-center of Fig. 8(b), the budding appears to be associated with twin (111) facets which form spontaneously during growth.

IV. DISCUSSION

We have developed a computationally efficient method to carry out molecular dynamics simulations of the deposition and growth of thin-films for large deposition angle. Since the entire system is included at every stage of the simulation, multiple scattering events which occur at large deposition angles are easily taken into account. Using this method, we have carried out large-scale simulations of Cu/Cu(100) growth for deposition angles ranging from 50° to 85° for both fixed and random azimuthal angle with a deposition rate corresponding to 0.3 ML/ns.

In agreement with experiments, for large deposition angles ($\theta \geq 80°$), we find well-defined columnar growth with vertical (tilted) columns for random (fixed) ϕ. In this case, for both random and fixed ϕ, we have also found that while the strain is initially compressive, it becomes tensile after the onset of columnar growth for large deposition angles, in good qualitative agreement with the behavior obtained previously by Zepeda-Ruiz *et al.*[10] in sputter-deposition experiments on Be growth with and without substrate bias. For fixed ϕ and $\theta = 70° - 85°$, we have also found reasonable agreement between the measured tilt angle and experiments on Ta_2O_5 and TiO_2 growth by Suzuki and Taga.[5] In addition, for large deposition angles, our results for the thin-film porosity were found to be in good agreement with recent experimental values for oxides[18] as well as for Cr.[19] However, our porosity results are significantly higher than is found experimentally for Cu.[19] This is consistent with the fact that—due to the high deposition rate used in our simulations—our simulations are more relevant to experiments carried out with significantly lower deposition rates but at lower homologous temperatures.

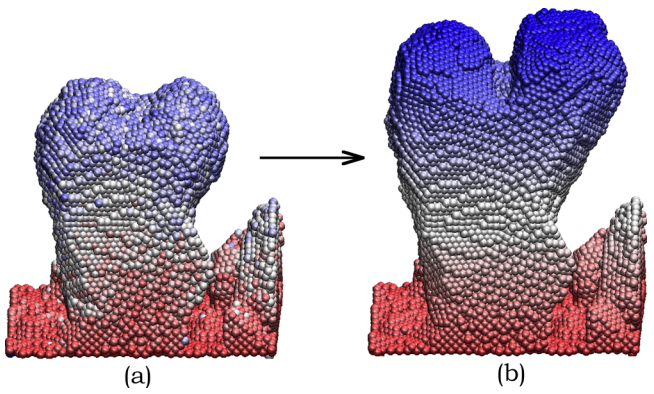

FIG. 13. Sequence of pictures at (a) 13.5 ML and (b) 17.25 ML showing budding for $\theta = 85^o$ with random ϕ. Color scheme indicates height of atoms above substrate.

In contrast, for smaller deposition angles ($\theta = 50°$ and 60°), columnar growth is not observed up to the maximum coverage (20 ML) studied in our simulations. Instead, primarily ridge-like behavior is observed in good agreement with previous MD and temperature-accelerated dynamics results,[7] while the average strain remains compressive. For these angles, our simulated porosities are somewhat higher than experimental values, perhaps due to the fact that columnar growth has not yet set in at these thicknesses.

For all deposition angles, we find large values of the surface roughness growth exponent β, where $\beta \simeq 1$ for the case of random ϕ while $\beta \simeq 0.6 - 1$ for fixed ϕ. In addition, for random azimuthal angle and large deposition angles ($\theta = 80°$ and 85°), the coarsening exponent $n \simeq 1/2$ is in good agreement with previous GLAD simulation results using a simplified cubic-lattice model without diffusion.[22] Thus, while dynamical effects, such as nanocolumn oscillations and large-scale re-arrangement events clearly enhance the coarsening, they do not appear to affect the coarsening exponent. However, for smaller deposition angles, the corresponding coarsening exponents ($n \simeq 0.2 - 0.33$) are consistent with GLAD simulation results previously obtained in the presence of surface diffusion.[22] This is also consistent with the fact that for small deposition angles, both the defect density and the number of re-arrangement events are significantly lower, while almost all of the film atoms correspond to the same (substrate) grain.

Due to the large deposition rate in our MD simulations, for high deposition angles, a large number of stacking faults are also observed leading to the formation of numerous grains and grain boundaries. In addition, the number of defects and grains, as well as the average non-substrate grain size increase with increasing deposition angle. However, as a result of deposition-induced events, the vacancy density remains extremely small (less than 0.1%) for all deposition angles. We note that this latter result is in contrast to the relatively large vacancy density obtained in kinetic Monte Carlo simulations of Be sputter deposition carried out using a lattice-based (but elastically relaxed) model at higher temperature (100 °C) which does not take into account deposition-induced events.

While these results indicate a complex dependence of the microstructure and morphology on deposition angle and film thickness, our simulations have also demonstrated the importance of two additional dynamical processes which may occur during glancing-angle deposition. In particular, our simulation results indicate that deposition fluctuations as well as large-scale re-arrangement events lead to large-

amplitude oscillations in the columnar growth regime. In addition, when two columns approach within a cutoff distance from one another, further large-scale re-arrangements occur followed by rapid coalescence, thus, enhancing the coarsening process. We have also found that in the case of large deposition angle θ and random azimuthal angle ϕ, splitting and/or budding of columns may occur. While this has been previously observed experimentally[17] as well as in previous MD simulations in which a single column with twin (111) facets was artificially created,[17] this twin-facet formation and budding occurs naturally in our simulations.

In conclusion, our simulations demonstrate that fully atomistic simulations are required in order to obtain an accurate description of many of the important processes which occur in glancing angle deposition. In particular, our simulations reveal that, on the MD time-scales studied here, glancing angle deposition is a very dynamic process involving surprisingly large re-arrangement and coalescence events which dramatically influence the thin-film morphology. In addition, the existence of deposition-induced events due to the energy of condensation of depositing atoms significantly reduces the vacancy density despite the existence of a large defect density. In the future, it would be interesting to combine our "parallel" MD simulations with parallel temperature-accelerated dynamics simulations,[7,34] in order to study the evolution of the thin-film morphology and microstructure over longer time- and length-scales.

ACKNOWLEDGMENTS

This research was supported by NSF Grant No. DMR-0907399 as well as by the University of Toledo Wright Center for Photovoltaic Innovation and Commercialization (PVIC). J.G.A. also received support from the Air Force Research Laboratory under Contract No. FA9453-08-C-0172 as well as a grant of computer time from the Ohio Supercomputer Center.

[1]Y. Zhao, D. Ye, G. Wang, and T. Lu, Proc. SPIE **5219**, 59 (2003).
[2]M. M. Hawkeye and M. J. Brett, J. Vac. Sci. Technol. A **25**, 1317 (2007).
[3]F. Favier, E. C. Walter, M. P. Zach, T. Benter, and R. M. Penner, Science **293**, 2227 (2001).
[4]T. Smy, D. Vick, M. J. Brett, S. K. Dew, A. T. Wu, J. C. Sit, and K. D. Harris, J. Vac. Sci. Technol. A **18**, 2507 (2000).
[5]M. Suzuki and Y. Taga, J. Appl. Phys. **90**, 5599 (2001).
[6]F. Montalenti and A. F. Voter. Phys. Rev. B **64**, 081401 (2001).
[7]Y. Shim, V. Borovikov, B. P. Uberuaga, A. F. Voter, and J. G. Amar, Phys. Rev. Lett. **101**, 116101 (2008).
[8]J. E. Rubio, M. Jaraiz, I. Martin-Bragado, J. M. Hernandez-Mangas, J. Barbolla, and G. H. Gilmer, J. Appl. Phys. **94**, 163 (2003).
[9]S. Mukherjee, C. M. Zhou, and D. Gall, J. Appl. Phys. **105**, 094318 (2009).
[10]L. A. Zepeda-Ruiz, E. Chason, G. H. Gilmer, Y. Wang, H. Xu, A. Nikroo, and A. V. Hamza, Appl. Phys. Lett. **95**, 151910 (2009).
[11]M. S. Daw and M. I. Baskes, Phys. Rev. B **29**, 6443 (1984).
[12]Y. Mishin, M. J. Mehl, D. A. Papaconstantopoulos, A. F. Voter, and J. D. Kress, Phys. Rev. B **63**, 224106 (2001).
[13]J. A. Anderson, C. D. Lorenz, and A. Travesset, J. Comput. Phys. **227**, 5342 (2008).
[14]See http://codeblue.umich.edu/hoomd-blue for HOOMD-blue code and documentaion.
[15]I. V. Morozov, A. M. Kazennov, R. G. Bystryi, G. E. Norman, V. V. Pisarev, and V. V. Stegailov, Comput. Phys. Commun. **182**, 1974 (2011).
[16]C. L. Kelchner, S. J. Plimpton, and J. C. Hamilton, Phys. Rev. B **58**, 11085 (1998).
[17]J. Wang, H. Huang, S. V. Kesapragada, and D. Gall, Nano Lett. **5**, 2505 (2005).
[18]D. J. Poxson, F. W. Mont, M. F. Schubert, J. K. Kim, and E. F. Schubert, Appl. Phys. Lett. **93**, 101914 (2008).
[19]K. Robbie and M. J. Brett, J. Vac. Sci. Technol. A **15**, 1460 (1997).
[20]Y. Shim, M. E. Mills, V. Borovikov, and J. G. Amar, Phys. Rev. E **79**, 051604 (2009).
[21]M. Backholm, M. Foss, and K. Nordlund, Nanotechnology **23**, 385708 (2012).
[22]T. Karabacak, J. P. Singh, Y. P. Zhao, G.-C. Wang, and T.-M. Lu, Phys. Rev. B **68**, 125408 (2003).
[23]S. J. Liu, H. C. Huang, and C. H. Woo, Appl. Phys. Lett. **80**, 3295 (2002).
[24]M.-C. Marinica, C. Barreteau, M.-C. Desjonqueres, and D. Spanjaard, Phys. Rev. B **70**, 075415 (2004).
[25]J. Repp, G. Meyer, K. H. Rieder, and P. Hyldgaard, Phys. Rev. Lett. **91**, 206102 (2003).
[26]J. Yu and J. G. Amar, Phys. Rev. Lett. **89**, 286103 (2002).
[27]J. Yu and J. G. Amar, Phys. Rev. B **69**, 045426 (2004).
[28]M. Karimi, T. Tomkowski, G. Vidali, and O. Biham, Phys. Rev. B **52**, 5364 (1995).
[29]C.-W. Pao, S. M. Foiles, E. B. Webb, D. J. Srolovitz, and J. A. Floro, Phys. Rev. Lett. **99**, 036102 (2007).
[30]R. W. Hoffman, Thin Solid Films **34**, 185 (1976).
[31]H. J. Butt and M. Jaschke, Nanotechnology **6**, 1 (1995).
[32]G. Ehrlich and F. G. Hudda, J. Chem. Phys. **44**, 1039 (1966).
[33]R. L. Schwoebel and E. J. Shipsey, J. Appl. Phys. **37**, 3682 (1966).
[34]Y. Shim, J. G. Amar, B. P. Uberuaga, and A. F. Voter, Phys. Rev. B **76**, 205439 (2007).